Spectroscopic view of ultrafast charge carrier dynamics in single- and bilayer transition metal dichalcogenide semiconductors

Paulina Majchrzak [a], Klara Volckaert [a], Antonija Grubišić Čabo [b], Deepnarayan Biswas [a], Marco Bianchi [a], Sanjoy K. Mahatha [c], Maciej Dendzik [b], Federico Andreatta [a], Signe S. Grønborg [a], Igor Marković [d,e], Jonathon M. Riley [d], Jens C. Johannsen [f], Daniel Lizzit [g], Luca Bignardi [h], Silvano Lizzit [i], Cephise Cacho [j], Oliver Alexander [k], Dan Matselyukh [k], Adam S. Wyatt [k], Richard T. Chapman [k], Emma Springate [k], Jeppe V. Lauritsen [a], Phil D.C. King [d], Charlotte E. Sanders [a], Jill A. Miwa [a], Philip Hofmann [a], Søren Ulstrup [a,*]

[a] *Department of Physics and Astronomy, Interdisciplinary Nanoscience Center, Aarhus University, 8000 Aarhus C, Denmark*
[b] *Department of Applied Physics, KTH Royal Institute of Technology, Hannes Alfvéns väg 12, 114 19 Stockholm, Sweden*
[c] *Ruprecht Haensel Laboratory, Deutsches Elektronen-Synchrotron DESY, 22607 Hamburg, Germany*
[d] *SUPA, School of Physics and Astronomy, University of St Andrews, St Andrews KY16 9SS, United Kingdom*
[e] *Max Planck Institute for Chemical Physics of Solids, Nöthnitzer Str. 40, 01187 Dresden, Germany*
[f] *Institute of Condensed Matter Physics, École Polytechnique Fédérale de Lausanne (EPFL), Switzerland*
[g] *DPIA, University of Udine, Via delle Scienze 206, 33100 Udine, Italy*
[h] *Department of Physics, University of Trieste, Via Valerio 2, Trieste 34127, Italy*
[i] *Elettra-Sincrotrone Trieste S.C.p.A., S.S. 14 km 163.5, 34149 Trieste, Italy*
[j] *Diamond Light Source, Didcot, OX110DE, United Kingdom*
[k] *Central Laser Facility, STFC Rutherford Appleton Laboratory, Harwell, United Kingdom*

ARTICLE INFO

ABSTRACT

The quasiparticle spectra of atomically thin semiconducting transition metal dichalcogenides (TMDCs) and their response to an ultrafast optical excitation critically depend on interactions with the underlying substrate. Here, we present a comparative time- and angle-resolved photoemission spectroscopy (TR-ARPES) study of the transient electronic structure and ultrafast carrier dynamics in the single- and bilayer TMDCs MoS_2 and WS_2 on three different substrates: Au(111), Ag(111) and graphene/SiC. The photoexcited quasiparticle bandgaps are observed to vary over the range of 1.9–2.5 eV between our systems. The transient conduction band signals decay on a sub-50 fs timescale on the metals, signifying an efficient removal of photoinduced carriers into the bulk metallic states. On graphene, we instead observe a fast timescale on the order of 170 fs, followed by a slow dynamics for the conduction band decay in MoS_2. These timescales are explained by Auger recombination involving MoS_2 and in-gap defect states. In bilayer TMDCs on metals we observe a complex redistribution of excited holes along the valence band that is substantially affected by interactions with the continuum of bulk metallic states.

1. Introduction

Semiconducting transition metal dichalcogenides (TMDCs) in the $2H$ structural modification with the formula unit MX_2 (M = {Mo, W}; X = {S, Se}) have attracted sustained attention due to their indirect-to-direct bandgap crossover upon thinning to the single layer (SL) limit [1–3]. The bandstructure in this class of materials can additionally be externally tuned via strain [4,5], as well as doping via alkali adsorption [6–9], electrostatic gating [10–13] and substrate interactions [14–18]. Compared to conventional bulk semiconductors,

SL TMDCs exhibit exceptionally large exciton and trion binding energies due to reduced dielectric screening of Coulomb interactions in the 2D material [1,14,16,19–21]. Moreover, broken inversion symmetry in the trigonal prismatic unit cell of a SL provides a possibility for spin-selective excitation of carriers around the direct bandgap at the $\bar{K}$ and $\bar{K}'$ valleys of the materials using circularly polarized light [22–24]. The high degree of control over the electronic properties and strong light-matter interactions elevate semiconducting TMDCs to promising

---

candidates for realizing novel applications in photonics, optoelectronics and spintronics [25–28].

Successfully integrating TMDCs with such applications requires a complete understanding of interactions with the underlying substrate and precise control of the quasiparticle and free carrier dynamics induced by an optical excitation. It has been shown that metallic substrates strongly influence the bandstructure of the TMDCs. For example, an insulator-to-metal phase transition of SL WS_2 and MoS_2 has been observed on Ag(111) due to hybridization of TMDC bands with the underlying metallic states [29–31]. A significant substrate-induced bandgap renormalization has been observed in the TMDCs due to dielectric screening [14–16]. The optical pulse itself can also lead to bandgap renormalization by creating a large population of strongly screening free carriers [32–34]. Furthermore, the optoelectronic properties of TMDCs are sensitive to defects, which may be intentionally or inadvertently introduced during or post synthesis [35], and which play a role in the ultrafast dynamics [36–39].

Time- and angle-resolved photoemission spectroscopy (TR-ARPES) has provided important insights to the energy- and momentum-dependent ultrafast carrier dynamics of TMDCs, directly revealing renormalization of the quasiparticle bandgap and the associated free carrier dynamics in SL MoS_2 [34,40], as well as interlayer carrier injection in a heterostructure composed of SL WS_2 and graphene [41]. Control of spin- and valley-dynamics has been demonstrated via circular dichroism in polarization dependent TR-ARPES on SL WS_2 [24,42]. In contrast, interlayer interactions in bilayer (BL) MoS_2 have led to the visualization of a momentum-dependent linear dichroism effect [43]. Furthermore, layer- and valley-selective optical excitations and inter-valley scattering processes have been studied by TR-ARPES on bulk TMDCs [44–47].

Here, we present a comparative TR-ARPES study of single- and bilayers of MoS_2 and WS_2 on Au(111), Ag(111) and graphene/SiC substrates. We combine a new analysis of our previous TR-ARPES measurements of SL MoS_2/Au(111) [40], SL MoS_2/graphene [34], SL WS_2/Ag(111) [24] and BL MoS_2/Ag(111) [43] with new TR-ARPES results on BL WS_2/Au(111). We contrast the ultrafast dynamics in SL MoS_2 on the graphene substrate with samples supported on the metallic substrates. The photoexcited quasiparticle bandgaps are compared across these systems, demonstrating an overall variation in gap size of 0.6 eV. The impact on the carrier dynamics of shifting the valence band maximum (VBM) from $\bar{K}$ in a SL to $\bar{\Gamma}$ in a BL and the associated interplay with bulk metallic states are determined, resulting in a complex picture of excited hole scattering in BL TMDCs supported on metals. Our work emphasizes the strong substrate dependence of carrier dynamics in SL and BL TMDCs from the perspective of TR-ARPES, providing an outset for expanding this methodology to advanced heterostructures and devices based on the TMDCs.

2. Experimental

The synthesis of our TMDC SL and BL samples generally follows the procedure of evaporating Mo or W onto a given substrate in ultra-high vacuum, followed by annealing in a low background pressure of H_2S. For details we refer to Ref. [48] (MoS_2/graphene), Refs. [43,49,50] (MoS_2 on Au(111) and Ag(111)) and Refs. [29,51] (WS_2 on Au(111) and Ag(111)).

The TR-ARPES measurements were performed at Artemis at the Central Laser Facility, Rutherford Appleton Laboratory. The experimental setup is presented schematically in Fig. 1(a). All the samples were optically excited with a 2 eV pump pulse, which is near-resonant with the quasiparticle bandgaps of our systems. The fluence of the pump beam was kept at approximately 3.0 mJ/cm^2 in order to maximize the pump–probe signal while avoiding space–charge effects [52]. This is the laser fluence impinging on the sample, which is not corrected for the absorption of the different systems. All SL samples were probed with 25-eV extreme ultraviolet (XUV) pulses, while the BL samples

were probed with 32.5-eV pulses. The probe pulses in all cases were produced via high harmonic generation in an argon gas jet. Both pump and probe beams were kept linearly polarized in these measurements. The time, energy and angular resolution were approximately 40 fs, 400 meV and 0.2°, respectively. The photoemission intensity was collected along the $\bar{\Gamma}$-$\bar{K}$ high-symmetry direction of the hexagonal Brillouin zone (BZ), providing access to the dispersion around the direct bandgap at $\bar{K}$ of MoS_2 and WS_2, as sketched in Fig. 1(b).

3. Results and discussion

3.1. Snapshots of excited free carriers

We first survey the energy- and momentum-dependent changes to the photoemission intensity around $\bar{K}$ following optical excitation, comparing the systems sketched in Fig. 1(c). TR-ARPES spectra measured in equilibrium conditions before optical excitation ($\Delta t < 0$) are shown in Fig. 1(d). The changes following optical excitation are presented in Fig. 1(e) via the difference in photoemission intensity between the equilibrium spectra in Fig. 1(d) and the corresponding spectra taken shortly after the arrival of the pump pulse ($\Delta t = 40$ fs). The red/blue contrast corresponds to gain/loss signal, which stems from three primary effects: (i) Filling/depletion of excited electrons/holes in the associated states, (ii) rigid band shifts caused by renormalization of the bandgap, and (iii) linewidth broadening of the bands that reflects the optically induced change of intrinsic quasiparticle lifetime [53–55].

The intensity difference for SL MoS_2/graphene is dominated by the loss signal (blue) in the valence band (VB) accompanied by a stark gain signal (red) directly above it, indicating a rigid shift of the band position in addition to the expected depletion. A flat region of intensity depletion and gain appears pinned to E_F. This suggests that the excitation leads to a significant population of in-gap states (IGS) that arise from defects in the sample. The intensity difference in the IGS above E_F is mixed with that of the finite population of free carriers in the conduction band minimum (CBM) [34].

For SL MoS_2/Au(111), BL MoS_2/Ag(111) and SL WS_2/Ag(111), the difference spectra primarily display a localized gain of intensity in the conduction band (CB) and a corresponding loss in the VB around $\bar{K}$, consistent with the presence of excited free electrons and holes in these states. A faint gain signal immediately adjacent to the central loss region in the VB could emerge from either a minute rigid shift of the bands or a slight broadening effect caused by the optical excitation.

The intensity difference of BL WS_2/Au(111) appears more complex than for the other systems. In particular, the system displays a flat gain signal directly above E_F, indicating a prominent filling of IGS. Further above E_F, a localized gain signal is indicative of the local CBM of BL WS_2 at $\bar{K}$. The substantial gain/loss signal surrounding the VB indicates a more pronounced linewidth broadening in this system.

3.2. Extraction of photoexcited quasiparticle bandgaps

We obtain a quantitative estimate of the photoexcited direct bandgap, E_g, at $\bar{K}$ by analyzing energy distribution curves (EDCs) of the intensity difference, binned ±0.1 Å^{-1} around $\bar{K}$. The EDCs are presented via green curves in Fig. 2(a). A multi-peak fit to Voigt functions on a polynomial background (smooth curves) permit a decomposition of the EDCs into single component peaks, as shown via filled red (blue) areas that signify gain (loss) in the photoemission signal. These are referred to as gain and loss peaks in the following discussion. We choose to analyze EDCs of the intensity difference instead of EDCs obtained from the raw spectra, as the complex background signal, that strongly varies between the systems (see Fig. 1(d)), is removed in the difference spectra. This introduces a small error of maximum 40 meV when comparing the extracted band position of the difference and raw EDCs.

In the VB region, the EDC for SL MoS_2/graphene displays negative and positive peaks adjacent to each other. This is caused by a rigid
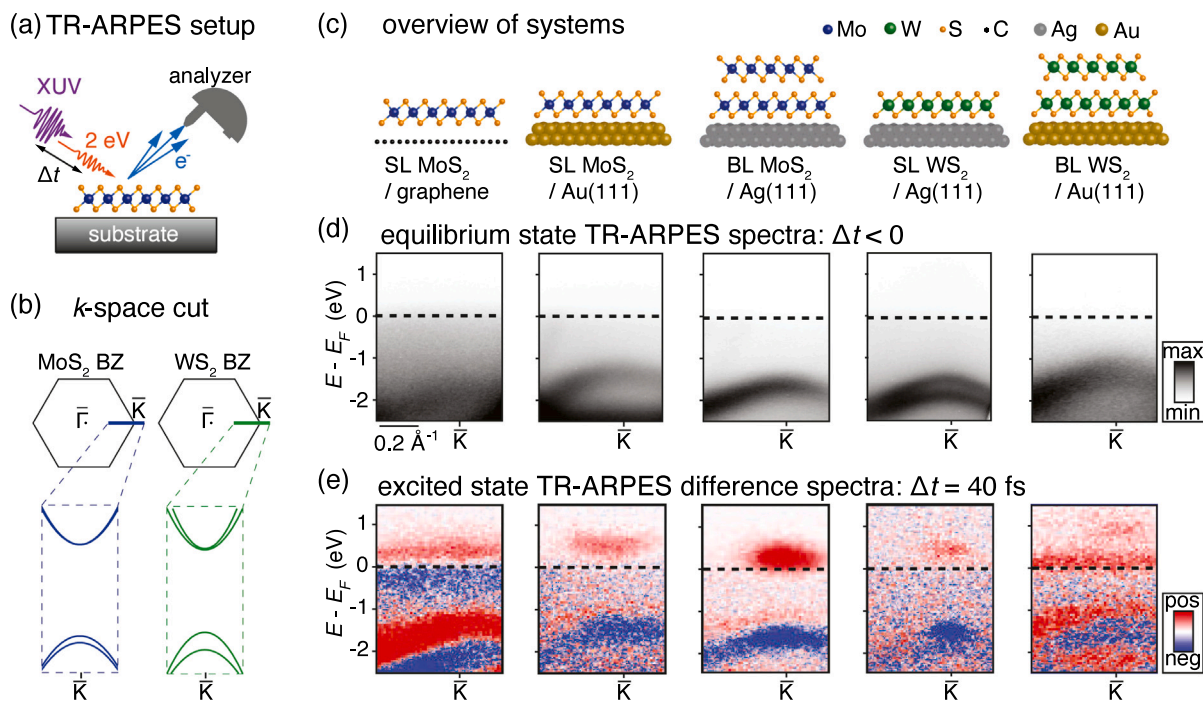
Fig. 1. (a) Sketch of TR-ARPES setup. (b) Brillouin zone (BZ) with TR-ARPES k-space cut indicated by blue and green lines for MoS_2 and WS_2, respectively. The cut provides access to the VB and CB dispersion around the direct gap of MoS_2 and WS_2, sketched within the dashed boxes. (c) Side-view diagrams of the systems studied in this work. (d) Photoemission intensity obtained for each system in equilibrium conditions before arrival of the pump pulse ($\Delta t < 0$). (e) Photoemission intensity difference at the peak of optical excitation ($\Delta t = 40$ fs). Each spectrum in (d)–(e) was obtained around $\bar{K}$ and corresponds to the system sketched in the same column in (c). The position of E_F is indicated by a horizontal dashed line.
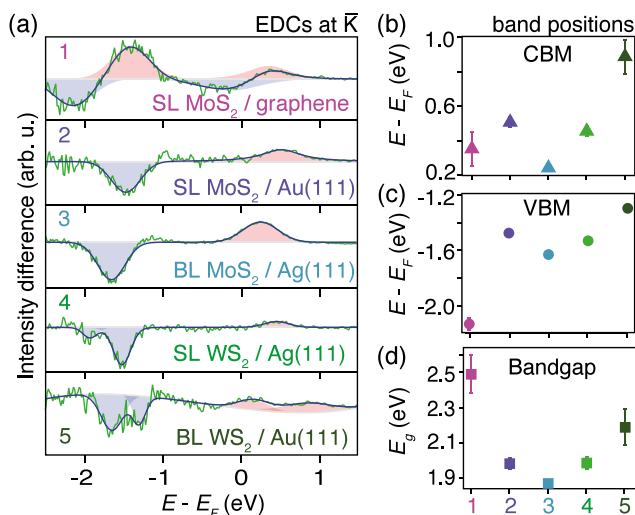

Fig. 2. (a) EDCs of the intensity difference (green curves) extracted by integrating the photoemission intensity difference over a region of ± 0.1 Å^{-1} around $\bar{K}$. The smooth curves represent fits to a multi-peak Voigt function on a polynomial background. Fitted peak components are shown via filled red (intensity gain) and blue (depletion) areas. (b)–(c) Positions of (b) CBM and (c) VBM extracted from the EDC analysis in (a). (d) Resulting direct bandgap at $\bar{K}$. The numbering of systems on the horizontal axis of (b)–(d) is referenced to the five systems in (a).

energy shift due to a bandgap renormalization induced by the photoinduced free carriers [34,56]. The VBM extracted from the equilibrium spectra coincides with the loss peak minimum. Around E_F, the larger amplitude of the gain peak compared to the loss peak is interpreted as a sign of the IGS superimposed on the excited CBM signal. We assume that the CBM coincides with the position of the gain peak maximum

above E_F. For the SL TMDCs and BL MoS_2 on metallic substrates, the isolated gain peaks above E_F clearly indicate the CBM energies. The VBM energies are obtained from the corresponding loss peaks below E_F. The slight broadening that is observed around the VB for these systems in Fig. 1(e) is accounted for in the fit via the polynomial background. In BL WS_2/Au(111), the two gain peaks above E_F permit us to separate the IGS and CBM by their positions in energy, IGS being the closest to E_F, for the further analysis. The two adjacent VB loss peaks observed for SL and BL WS_2 reflect the spin-split VB states that are separated by 420 meV [51].

The fitted peak positions corresponding to the CBM and VBM are presented in Figs. 2(b)–(c). For all the investigated samples, E_F is situated closer to the CBM than the VBM, indicating n-type doping. This is consistent with theoretical work, where the doping is attributed to the metal work function modification upon charge redistribution at the interface as well as the appearance of gap states of predominantly metallic d-orbital character [57,58]. We note that hybridization with substrate states can also shift and distort bands [15,59]. The VB at $\bar{K}$ is situated at a higher binding energy for MoS_2 and WS_2 samples supported on Ag(111) compared to their counterparts supported on Au(111), which is a result of Fermi level pinning due to different substrate work functions [29]. In SL MoS_2/graphene and BL WS_2/Au(111) the Fermi level is pinned by the IGS.

In Fig. 2(d), we show the size of the quasiparticle bandgaps determined from the VBM and CBM energies. For the MoS_2 samples, the value of the bandgap is slightly overestimated since we are unable to resolve the spin-splitting of 145 meV [6], moving the negative intensity difference peak to the middle of the split bands. The quasiparticle bandgap of ≈ 2.5 eV for the quasi-freestanding SL MoS_2 on graphene is significantly larger than that for samples on metallic supports due to weaker dielectric screening and absence of hybridization between TMDC and substrate electronic bands. In optically excited SL MoS_2/graphene, the bandgap is reduced by the free carrier density, which shifts the CB and VB towards each other [34]. For TMDCs on
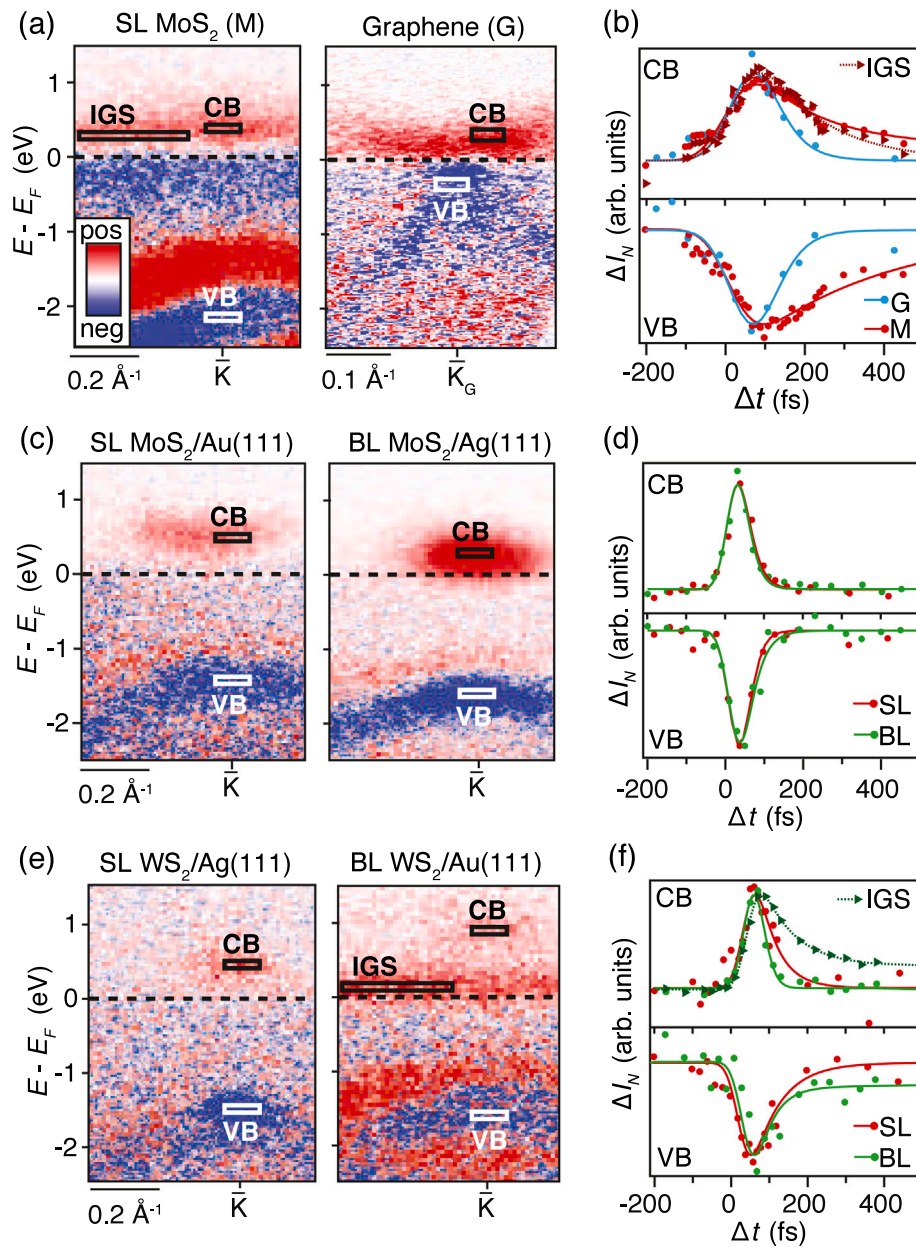
Fig. 3. (a) Intensity difference at the peak of excitation for (left) SL MoS$_2$/graphene and (right) underlying graphene around the Dirac point $\bar{K}_G$. (b) Integrated photoemission intensity difference (markers) as a function of time within the corresponding boxed regions shown in (a). Smooth curves represent fits to exponential functions convoluted with a Gaussian function that accounts for the temporal resolution. The dynamics in the CB and IGS of SL MoS$_2$/graphene are described by biexponential functions, while the other regions are described by single exponentials. (c)–(f) Similar analysis as in (a)–(b) presented for (c)–(d) SL MoS$_2$/Au(111) and BL MoS$_2$/Ag(111) and (e)–(f) SL WS$_2$/Ag(111) and BL WS$_2$/Au(111). In (f), the dynamics in the VB and IGS of BL WS$_2$/Au(111) are described by biexponential functions while the remaining dynamics are described by single exponentials.

metal supports, the bandgaps are substantially renormalized by the strong dielectric screening from the substrate, reaching a minimum of $\approx$1.9 eV. Interestingly, we observe a somewhat larger direct bandgap of $\approx$2.2 eV in BL WS$_2$/Au(111). This may be explained by the global minimum of the CB shifting away from $\bar{K}$ to the $\bar{\Sigma}$ valley between $\bar{\Gamma}$ and $\bar{K}$ in BL WS$_2$ [60], pushing the energy of the CB states at $\bar{K}$ further from the VB.

3.3. Analysis of carrier relaxation timescales

The time-dependent evolution of the excitation and ensuing recombination processes in our systems is investigated by integrating the

normalized intensity difference within boxes around the (E, k)-regions containing the CBM and VBM at $\bar{K}$, as well as an IGS region away from $\bar{K}$, as shown for each system in Figs. 3(a), 3(c) and 3(e). The resulting time-dependence of integrated intensity difference, denoted by ΔI_N, is shown for each system in Figs. 3(b), 3(d) and 3(f). The characteristic decay time constants of the signals for each system are extracted by fitting with exponential functions convoluted with a Gaussian temporal resolution function. The resulting decay constants for the CBM, VBM and IGS regions are summarized in Table 1 and discussed further below.

In SL MoS$_2$/graphene the VB signal is described by a single exponential function with time constant (355 ± 37) fs, while the CB signal is described by a fast decay of (171 ± 28) fs followed by a slow dynamics

Table 1

Relaxation timescales resulting from the fits in Figs. 3(b), 3(d) and 3(f). The quasiparticle bandgaps resulting from the analysis in Fig. 2(d) have been added for completeness.

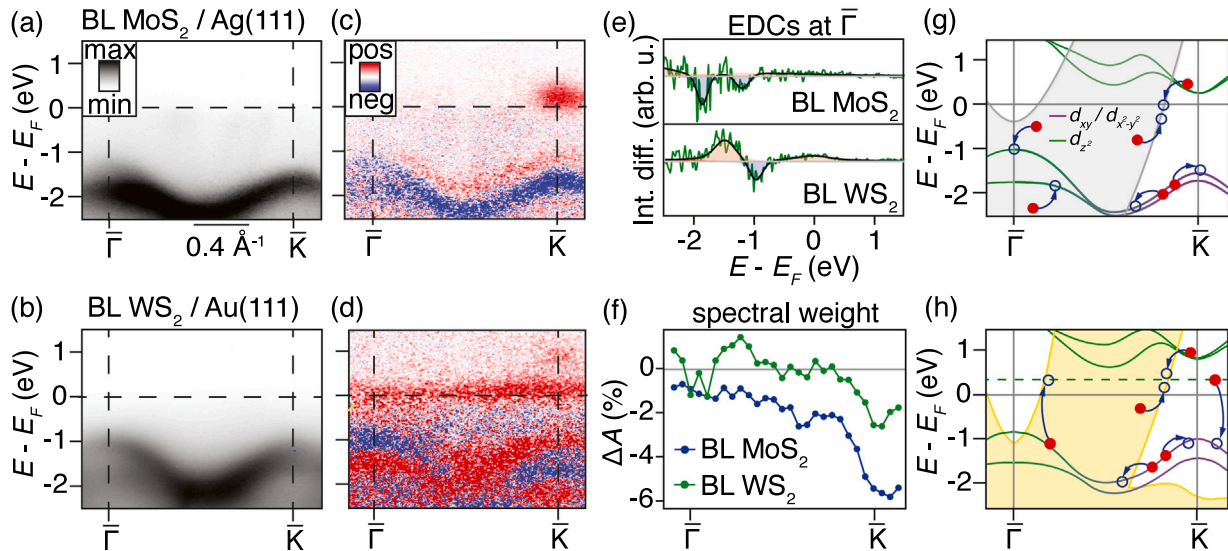| System	E_g (eV)	τ_{CB} (fs)	τ_{VB} (fs)	τ_{IGS} (fs)
SL MoS$_2$/graphene	2.33 ± 0.10	171 ± 28	355 ± 37	157 ± 23
SL MoS$_2$/Au(111)	2.00 ± 0.04	33 ± 20	30 ± 20	–
BL MoS$_2$/Ag(111)	1.89 ± 0.01	34 ± 20	30 ± 20	–
SL WS$_2$/Ag(111)	1.92 ± 0.05	49 ± 20	72 ± 34	–
BL WS$_2$/Au(111)	2.19 ± 0.18	30 ± 20	43 ± 20	84 ± 27

Fig. 4. (a)–(b) ARPES intensity of (a) BL MoS$_2$/Ag(111) and (b) BL WS$_2$/Au(111) along $\bar{\Gamma}$-$\bar{K}$ before optical excitation. (c)–(d) Corresponding intensity difference between spectra acquired at the peak of excitation ($\Delta t \approx 40$ fs) and the equilibrium spectra in (a)–(b). (e) EDCs (green curves) of the intensity difference obtained at $\bar{\Gamma}$ in (c)–(d). Smooth curves represent multi-peak Voigt function fits with fitted peak components shown via filled red (intensity gain) and blue (depletion) areas. (f) Change of spectral weight along the VB between equilibrium and peak excitation. (g)–(h) Schematic representation of possible electron (filled red circles) and hole (empty blue circles) recombination processes. In (g) the BL MoS$_2$ bandstructure is sketched and color-coded according to the orbital character of the bands, based on calculations from Refs. [61–63]. In (h), the similar sketch of the BL WS$_2$ bandstructure is based on the calculations in Refs. [60,62]. The dashed horizontal line indicates the IGS. Gray and yellow shading in (g)–(h) represent the projected bulk bandstructure of Ag(111) and Au(111), respectively, adapted from Refs. [29,64].

that extends outside our detection window. The different timescales are caused by slow- and fast-acting recombination mechanisms between the CB, VB and IGS states [36]. The time-dependence of the corresponding excitation and relaxation processes in the underlying graphene in the boxes around the Dirac cone at $\bar{K}_G$, shown in Fig. 3(a), is inspected in order to determine whether there is any charge transfer between MoS$_2$ and graphene. We observe that the electron and hole signals are highly symmetric in graphene, the rise-time of the signals is identical with what we see in MoS$_2$, and the subsequent relaxation is much faster in graphene. These observations do not clearly indicate charge transfer processes, however, we cannot rule out that such charge transfer dynamics is faster than we can resolve or that the associated signals would evade observation with our signal-to-noise ratio. We also note that the graphene and MoS$_2$ lattices are predominantly rotated by 30° with respect to each other as the result of our growth method [48], preventing hybridization between the Dirac cone and the MoS$_2$ VBM and CBM states and thereby removing any efficient charge transfer channels.

In MoS$_2$ on metallic substrates and SL WS$_2$ on Ag(111), the recombination dynamics is significantly faster. For SL and BL MoS$_2$, the signal is symmetric between VB and CB. It can be described with a single decay constant around 30 fs, which is comparable to our time-resolution. In SL WS$_2$, the extracted decay time is slightly higher, ≈50 fs for the CB and ≈70 fs for the VB. These ultrafast relaxation processes proceed via electron–hole pair recombination involving the bulk continuum of states in the metal substrates [40]. For BL WS$_2$/Au(111) the excited CB signal displays a similar ultrafast decay. However, the VB and IGS

signals are described by a fast component that is ≈40 fs for the VB and ≈80 fs for the IGS, followed by a slow decay that is outside our detection window.

In all the systems considered here, the decay of photoexcited carriers proceeds several orders of magnitude faster than in large bandgap bulk semiconductors, where the direct band-to-band recombination of the photoexcited carriers occurs on timescales varying from hundreds of picoseconds in GaAs [65], to tens of nanoseconds in rutile TiO$_2$ [66].

3.4. Dynamics along $\bar{\Gamma}$-$\bar{K}$ in bilayers

In bilayer TMDCs, the interaction of the out-of-plane orbitals between the two layers causes a bonding–antibonding splitting of the VB states at $\bar{\Gamma}$, which ultimately shifts the VBM to $\bar{\Gamma}$ [49,60,61,63]. By analyzing TR-ARPES spectra obtained along the full $\bar{\Gamma}$-$\bar{K}$ line we are able to evaluate how the shift of the VBM away from $\bar{K}$ influences carrier dynamics in the BL systems.

In Figs. 4(a)–(b), we present ARPES spectra along $\bar{\Gamma}$-$\bar{K}$ of BL MoS$_2$/Ag(111) and BL WS$_2$/Au(111) taken before the arrival of the pump pulse. The primary distinction between the two systems is that the VBM at $\bar{\Gamma}$ is clearly visible in WS$_2$, but faded in MoS$_2$ as a consequence of photoemission matrix element effects. The corresponding difference spectra between equilibrium and peak excitation spectra are shown in Figs. 4(c)–(d). EDCs of the intensity difference at $\bar{\Gamma}$ are presented in Fig. 4(e), following a similar analysis as for the corresponding EDCs at $\bar{K}$ in Fig. 2(a). The VB splitting is evident in BL MoS$_2$ in the intensity difference, leading to a value of (690±30) meV via

our fits of the EDCs. For BL WS_2 we determine a value for the splitting of (680 ± 20) meV from the raw spectrum in Fig. 4(b).

We determine the change of spectral weight, ΔA, along the VB by extracting EDCs of the raw TR-ARPES spectra and calculate the change of the area under the VB peak between equilibrium and excited state EDCs. We perform this EDC analysis at each k between $\bar{\Gamma}$ and $\bar{K}$ in bins of ± 0.1 Å^{-1}. The value ΔA is proportional to the number of excited holes in a given part of the band [34], neglecting any optically induced changes to the photoemission matrix element effects [43,67,68]. The extracted dependence of ΔA on k is presented in Fig. 4(f). In BL MoS_2/Ag(111), the signal from excited holes peaks around $\bar{K}$, and is significantly reduced, but not removed, along the band towards $\bar{\Gamma}$. This appears rather surprising as one would anticipate the holes to accumulate around the minimum energy state at the VBM at $\bar{\Gamma}$. A possible explanation involves the change of orbital character of the bands from $\bar{K}$ to $\bar{\Gamma}$ and the location of bulk states of the Ag(111) substrate, which are summarized in Fig. 4(g). At $\bar{K}$ the in-plane $d_{xy}/d_{x^2-y^2}$ orbital character of the VB results in weaker coupling to the substrate compared to the out-of-plane d_{z^2} orbital character around $\bar{\Gamma}$ [62,63,69]. Moreover, the latter states are fully overlapped in energy and momentum with metallic bulk states, facilitating efficient hybridization between these BL MoS_2 states and the substrate. Electron–hole recombination processes involving these states therefore proceed efficiently via Auger processes, as sketched in Fig. 4(g).

In BL WS_2/Au(111), the photoexcited holes in the VB have competing scattering channels available: They can either decay into the metallic states, or they can recombine with the IGS, as seen via the time dependent dynamics in Fig. 3(f). Furthermore, the energy- and momentum-dependence of the bulk continuum of metallic states in Au(111) leads to a peculiar situation where the states at the VBM of BL WS_2 are located in the projected bulk gap of the Au(111) at $\bar{\Gamma}$, as shown in Fig. 4(h). This leads to a less efficient coupling with the substrate and a peaked concentration of holes at the top of the VB, which is seen via the loss signals around -1 eV in Figs. 4(d)–(e) and the spikes in the green curve at $\bar{\Gamma}$ in Fig. 4(f). The remaining gain signals likely result from the additional IGS scattering channels.

Our analysis thus reveals a complex dependence of carrier dynamics in BL TMDCs on the interaction with underlying substrate states and the orbital characters of the TMDC VB states. When considering the consequences of this dynamics for the use of the SL semiconductors in devices, the efficient removal of carriers demonstrated on the metal substrates would be advantageous around electrodes in a device based on TDMCs. On the other hand, clean access to the ultrafast dynamics of TMDCs along the entire top-most VB requires substrates without electronic states in this region, such as oxide insulators [70] or hexagonal boron nitride [9].

4. Conclusion and outlook

In summary, we have determined the influence of graphene, Au(111) and Ag(111) substrates and the presence of IGS on the ultrafast dynamics of SL and BL MoS_2 and WS_2. On Au(111) and Ag(111), the quasiparticle bandgap is significantly reduced, reaching ≈ 1.9 eV, compared to the value of ≈ 2.5 eV determined on the graphene substrate. In the TMDCs supported on metals we found an ultrafast relaxation of the signal on the order of our 40 fs time-resolution. This behavior reflects the efficient electron–hole pair recombination channels provided by the substrates. On the weakly-interacting graphene the dynamics in the adjacent SL MoS_2 was more strongly dominated by interactions with IGS that led to a fast timescale on the order of 170 fs followed by a slow decay in the CB states.

In the future, we hope to extend this work to TMDC samples on insulating substrates such as metal oxides [70,71], as well as TMDC-based heterostructures [58,72]. Indeed, TR-ARPES studies on SL semiconducting TMDCs have until recently been limited by flake sizes that are small (on the order of 10 μm) compared to the typical XUV beam size. As the TMDC growth technology is maturing, synthesis of large, single-orientation MoS_2 and WS_2 flakes has become possible on a range of substrates [50,71,73], and a variety of sample infrastructures can be engineered by van der Waals pick-up transfer methods [74]. Furthermore, the application of photoemission electron microscopes to pump–probe experiments [75,76] allows for the combination of time- and momentum-resolved spectra with imagining at the microscale. A full understanding of the nuanced interfacial interactions on the electronic structure of the TMDCs and their heterostructures will have an invaluable impact for tailoring optoelectronic devices.

The research data supporting this publication can be accessed at https://doi.org/10.17630/fcadc584-fdd7-4b8b-ae68-371135564c0c

Declaration of competing interest

The authors declare that they have no known competing financial interests or personal relationships that could have appeared to influence the work reported in this paper.

Acknowledgments

References

[1] K.F. Mak, C. Lee, J. Hone, J. Shan, T.F. Heinz, Phys. Rev. Lett. 105 (2010) 136805.

[2] W. Zhao, Z. Ghorannevis, L. Chu, M. Toh, C. Kloc, P.-H. Tan, G. Eda, ACS Nano 7 (2013) 791.

[3] Y. Zhang, T.-R. Chang, B. Zhou, Y.-T. Cui, H. Yan, Z. Liu, F. Schmitt, J. Lee, R. Moore, Y. Chen, H. Lin, H.-T. Jeng, S.-K. Mo, Z. Hussain, A. Bansil, Z.-X. Shen, Nature Nanotechnol. 9 (2014) 111.

[4] J. Feng, X. Qian, C.-W. Huang, J. Li, Nat. Photonics 6 (2012) 866.

[5] P. Johari, V.B. Shenoy, ACS Nano 6 (2012) 5449.

[6] J.A. Miwa, S. Ulstrup, S.G. Sørensen, M. Dendzik, A.G. Čabo, M. Bianchi, J.V. Lauritsen, P. Hofmann, Phys. Rev. Lett. 114 (2015a) 046802.

[7] Y. Zhang, M.M. Ugeda, C. Jin, S.-F. Shi, A.J. Bradley, A. Martín-Recio, H. Ryu, J. Kim, S. Tang, Y. Kim, B. Zhou, C. Hwang, Y. Chen, F. Wang, M.F. Crommie, Z. Hussain, Z.-X. Shen, S.-K. Mo, Nano Lett. 16 (2016) 2485.

[8] M. Kang, B. Kim, S.H. Ryu, S.W. Jung, J. Kim, L. Moreschini, C. Jozwiak, E. Rotenberg, A. Bostwick, K.S. Kim, Nano Lett. 17 (2017) 1610.

[9] J. Katoch, S. Ulstrup, R.J. Koch, S. Moser, K.M. McCreary, S. Singh, J. Xu, B.T. Jonker, R.K. Kawakami, A. Bostwick, E. Rotenberg, C. Jozwiak, Nat. Phys. 14 (2018) 355.

[10] A. Ramasubramaniam, D. Naveh, E. Towe, Phys. Rev. B 84 (2011) 205325.

[11] J.S. Ross, S. Wu, H. Yu, N.J. Ghimire, A.M. Jones, G. Aivazian, J. Yan, D.G. Mandrus, D. Xiao, W. Yao, X. Xu, Nature Commun. 4 (2013) 1474.

[12] A. Chernikov, A.M. van der Zande, H.M. Hill, A.F. Rigosi, A. Velauthapillai, J. Hone, T.F. Heinz, Phys. Rev. Lett. 115 (2015a) 126802.

[13] P.V. Nguyen, N.C. Teutsch, N.P. Wilson, J. Kahn, X. Xia, A.J. Graham, V. Kandyba, A. Giampietri, A. Barinov, G.C. Constantinescu, N. Yeung, N.D.M. Hine, X. Xu, D.H. Cobden, N.R. Wilson, Nature 572 (2019) 220.

[14] M.M. Ugeda, A.J. Bradley, S.-F. Shi, F.H. d. Jornada, Y. Zhang, D.Y. Qiu, W. Ruan, S.-K. Mo, Z. Hussain, Z.-X. Shen, F. Wang, S.G. Louie, M.F. Crommie, Nature Mater. 13 (2014) 1091.

[15] A. Bruix, J.A. Miwa, N. Hauptmann, D. Wegner, S. Ulstrup, S.S. Grønborg, C.E. Sanders, M. Dendzik, A.G. Čabo, M. Bianchi, J.V. Lauritsen, A.A. Khajetoorians, B. Hammer, P. Hofmann, Phys. Rev. B 93 (2016) 165422.

[16] A. Raja, A. Chaves, J. Yu, G. Arefe, H.M. Hill, A.F. Rigosi, T.C. Berkelbach, P. Nagler, C. Schüller, T. Korn, C. Nuckolls, J. Hone, L.E. Brus, T.F. Heinz, D.R. Reichman, A. Chernikov, Nature Commun. 8 (2017) 15251.

[17] S. Ulstrup, C.E. Giusca, J.A. Miwa, C.E. Sanders, A. Browning, P. Dudin, C. Cacho, O. Kazakova, D.K. Gaskill, R.L. Myers-Ward, T. Zhang, M. Terrones, P. Hofmann, Nature Commun. 10 (2019) 3283.

[18] L. Waldecker, A. Raja, M. Rösner, C. Steinke, A. Bostwick, R.J. Koch, C. Jozwiak, T. Taniguchi, K. Watanabe, E. Rotenberg, T.O. Wehling, T.F. Heinz, Phys. Rev. Lett. 123 (2019) 206403.

[19] K.F. Mak, K. He, C. Lee, G.H. Lee, J. Hone, T.F. Heinz, J. Shan, Nature Mater. 12 (2013) 207.

[20] A. Chernikov, T.C. Berkelbach, H.M. Hill, A. Rigosi, Y. Li, O.B. Aslan, D.R. Reichman, M.S. Hybertsen, T.F. Heinz, Phys. Rev. Lett. 113 (2014) 076802.

[21] Z. Ye, T. Cao, K. O'Brien, H. Zhu, X. Yin, Y. Wang, S.G. Louie, X. Zhang, Nature 513 (2014) 214.

[22] D. Xiao, G.-B. Liu, W. Feng, X. Xu, W. Yao, Phys. Rev. Lett. 108 (2012) 196802.

[23] K.F. Mak, K.L. McGill, J. Park, P.L. McEuen, Science 344 (2014) 1489 LP.

[24] S. Ulstrup, A.G. Čabo, D. Biswas, J.M. Riley, M. Dendzik, C.E. Sanders, M. Bianchi, C. Cacho, D. Matselyukh, R.T. Chapman, E. Springate, P.D.C. King, J.A. Miwa, P. Hofmann, Phys. Rev. B 95 (2017) 041405.

[25] Q.H. Wang, K. Kalantar-Zadeh, A. Kis, J.N. Coleman, M.S. Strano, Nature Nanotechnol. 7 (2012) 699.

[26] X. Xu, W. Yao, D. Xiao, T.F. Heinz, Nat. Phys. 10 (2014) 343.

[27] K.F. Mak, J. Shan, Nat. Photonics 10 (2016) 216.

[28] S.-J. Liang, B. Cheng, X. Cui, F. Miao, Adv. Mater. 32 (2020) 1903800.

[29] M. Dendzik, A. Bruix, M. Michiardi, A.S. Ngankeu, M. Bianchi, J.A. Miwa, B. Hammer, P. Hofmann, C.E. Sanders, Phys. Rev. B 96 (2017) 235440.

[30] G.M. d. Amaral, I. da Costa Tonon, R.J. Peña Román, H. de Oliveira Plath, T.M. Taniguchi, L.H. d. Lima, L.F. Zagonel, R. Landers, A. d. Siervo, Appl. Surf. Sci. 538 (2021) 148138.

[31] B.T. Blue, G.G. Jernigan, D. Le, J.J. Fonseca, S.D. Lough, J.E. Thompson, D.D. Smalley, T.S. Rahman, J.T. Robinson, M. Ishigami, 2D Mater. 7 (2020) 25021.

[32] A. Chernikov, C. Ruppert, H.M. Hill, A.F. Rigosi, T.F. Heinz, Nat. Photonics 9 (2015b) 466.

[33] E.A.A. Pogna, M. Marsili, D.D. Fazio, S. Da. Conte, C. Manzoni, D. Sangalli, D. Yoon, A. Lombardo, A.C. Ferrari, A. Marini, G. Cerullo, D. Prezzi, ACS Nano, ACS Nano 10 (2016) 1182.

[34] S. Ulstrup, A.G. Čabo, J.A. Miwa, J.M. Riley, S.S. Grønborg, J.C. Johannsen, C. Cacho, O. Alexander, R.T. Chapman, E. Springate, M. Bianchi, M. Dendzik, J.V. Lauritsen, P.D.C. King, P. Hofmann, ACS Nano 10 (2016a) 6315.

[35] H.R. Gutiérrez, N. Perea-López, A.L. Elías, A. Berkdemir, B. Wang, R. Lv, F. López-Urías, V.H. Crespi, H. Terrones, M. Terrones, Nano Lett. 13 (2013) 3447.

[36] H. Wang, C. Zhang, F. Rana, Nano Lett. 15 (2015) 339.

[37] L. Li, M.-F. Lin, X. Zhang, A. Britz, A. Krishnamoorthy, R. Ma, R.K. Kalia, A. Nakano, P. Vashishta, P. Ajayan, M.C. Hoffmann, D.M. Fritz, U. Bergmann, O.V. Prezhdo, Nano Lett. 19 (2019) 6078.

[38] Y. Li, W. Liu, Y. Wang, Z. Xue, Y.-C. Leng, A. Hu, H. Yang, P.-H. Tan, Y. Liu, H. Misawa, Q. Sun, Y. Gao, X. Hu, Q. Gong, Nano Lett. 20 (2020) 3747.

[39] H. Liu, C. Wang, Z. Zuo, D. Liu, J. Luo, Adv. Mater. 32 (2020) 1906540.

[40] A.G. Čabo, J.A. Miwa, S.S. Grønborg, J.M. Riley, J.C. Johannsen, C. Cacho, O. Alexander, R.T. Chapman, E. Springate, M. Grioni, J.V. Lauritsen, P.D.C. King, P. Hofmann, S. Ulstrup, Nano Lett. 15 (2015) 5883.

[41] S. Aeschlimann, A. Rossi, M. Chávez-Cervantes, R. Krause, B. Arnoldi, B. Stadtmüller, M. Aeschlimann, S. Forti, F. Fabbri, C. Coletti, I. Gierz, Sci. Adv. 6 (2020) eaay0761.

[42] H. Beyer, G. Rohde, A.G. Čabo, A. Stange, T. Jacobsen, L. Bignardi, D. Lizzit, P. Lacovig, C.E. Sanders, S. Lizzit, K. Rossnagel, P. Hofmann, M. Bauer, Phys. Rev. Lett. 123 (2019) 236802.

[43] K. Volckaert, H. Rostami, D. Biswas, I. Marković, F. Andreatta, C.E. Sanders, P. Majchrzak, C. Cacho, R.T. Chapman, A. Wyatt, E. Springate, D. Lizzit, L. Bignardi, S. Lizzit, S.K. Mahatha, M. Bianchi, N. Lanata, P.D.C. King, J.A. Miwa, A.V. Balatsky, P. Hofmann, S. Ulstrup, Phys. Rev. B 100 (2019) 241406.

[44] P. Hein, A. Stange, K. Hanff, L.X. Yang, G. Rohde, K. Rossnagel, M. Bauer, Phys. Rev. B 94 (2016) 205406.

[45] R. Wallauer, J. Reimann, N. Armbrust, J. Güdde, U. Höfer, Appl. Phys. Lett. 109 (2016) 162102.

[46] R. Bertoni, C.W. Nicholson, L. Waldecker, H. Hübener, C. Monney, U. De Giovannini, M. Puppin, M. Hoesch, E. Springate, R.T. Chapman, C. Cacho, M. Wolf, A. Rubio, R. Ernstorfer, Phys. Rev. Lett. 117 (2016) 277201.

[47] R. Wallauer, P. Marauhn, J. Reimann, S. Zoerb, F. Kraus, J. Güdde, M. Rohlfing, U. Höfer, Phys. Rev. B 102 (2020) 125417.

[48] J.A. Miwa, M. Dendzik, S.S. Grønborg, M. Bianchi, J.V. Lauritsen, P. Hofmann, S. Ulstrup, ACS Nano 9 (2015b) 6502.

[49] S.S. Grønborg, S. Ulstrup, M. Bianchi, M. Dendzik, C.E. Sanders, J.V. Lauritsen, P. Hofmann, J.A. Miwa, Langmuir 31 (2015) 9700.

[50] H. Bana, E. Travaglia, L. Bignardi, P. Lacovig, C.E. Sanders, M. Dendzik, M. Michiardi, M. Bianchi, D. Lizzit, F. Presel, D. De Angelis, N. Apostol, P. Kumar Das, J. Fujii, I. Vobornik, R. Larciprete, A. Baraldi, P. Hofmann, S. Lizzit, 2D Mater. 5 (2018) 035012.

[51] M. Dendzik, M. Michiardi, C. Sanders, M. Bianchi, J.A. Miwa, S.S. Grønborg, J.V. Lauritsen, A. Bruix, B. Hammer, P. Hofmann, Phys. Rev. B 92 (2015) 245442.

[52] S. Ulstrup, J.C. Johannsen, F. Cilento, A. Crepaldi, J.A. Miwa, M. Zacchigna, C. Cacho, R.T. Chapman, E. Springate, F. Fromm, C. Raidel, T. Seyller, P.D. King, F. Parmigiani, M. Grioni, P. Hofmann, J. Electron Spectrosc. Relat. Phenom. 200 (2015a) 340, special Anniversary Issue: Volume 200.

[53] S. Ulstrup, J. Christian Johannsen, A. Crepaldi, F. Cilento, M. Zacchigna, C. Cacho, R.T. Chapman, E. Springate, F. Fromm, C. Raidel, T. Seyller, F. Parmigiani, M. Grioni, P. Hofmann, J. Phys.: Condens. Matter 27 (2015b) 164206.

[54] M.X. Na, A.K. Mills, F. Boschini, M. Michiardi, B. Nosarzewski, R.P. Day, E. Razzoli, A. Sheyerman, M. Schneider, G. Levy, S. Zhdanovich, T.P. Devereaux, A.F. Kemper, D.J. Jones, A. Damascelli, Science 366 (2019) 1231.

[55] P. Majchrzak, S. Pakdel, D. Biswas, A.J.H. Jones, K. Volckaert, I. Marković, F. Andreatta, R. Sankar, E. Rotenberg, A. Bostwick, C.E. Sanders, Y. Zhang, G. Karras, R.T. Chapman, A. Wyatt, E. Springate, J.A. Miwa, P. Hofmann, P.D.C. King, N. Lanata, Y.J. Chang, S. Ulstrup, Phys. Rev. B 103 (2021) L241108.

[56] A. Steinhoff, M. Rösner, F. Jahnke, T.O. Wehling, C. Gies, Nano Lett. 14 (2014) 3743.

[57] I. Popov, G. Seifert, D. Tománek, Phys. Rev. Lett. 108 (2012) 156802.

[58] C. Gong, L. Colombo, R.M. Wallace, K. Cho, Nano Lett. 14 (2014) 1714.

[59] B. Shao, A. Eich, C. Sanders, A.S. Ngankeu, M. Bianchi, P. Hofmann, A.A. Khajetoorians, T.O. Wehling, Nature Commun. 10 (2019) 180.

[60] H. Zeng, G.-B. Liu, J. Dai, Y. Yan, B. Zhu, R. He, L. Xie, S. Xu, X. Chen, W. Yao, X. Cui, Sci. Rep. 3 (2013) 1608.

[61] T. Cheiwchanchamnangij, W.R.L. Lambrecht, Phys. Rev. B 85 (2012) 205302.

[62] A. Kormányos, G. Burkard, M. Gmitra, J. Fabian, V. Zólyomi, N.D. Drummond, V. Fal'ko, 2D Mater. 2 (2015) 022001.

[63] A. Kormányos, V. Zólyomi, V.I. Fal'ko, G. Burkard, Phys. Rev. B 98 (2018) 035408.

[64] N. Takeuchi, C.T. Chan, K.M. Ho, Phys. Rev. B 43 (1991) 13899.

[65] A. Othonos, J. Appl. Phys. 83 (1998) 1789.

[66] Y. Yamada, Y. Kanemitsu, Appl. Phys. Lett. 101 (2012) 133907.

[67] H. Rostami, K. Volckaert, N. Lanata, S.K. Mahatha, C.E. Sanders, M. Bianchi, D. Lizzit, L. Bignardi, S. Lizzit, J.A. Miwa, A.V. Balatsky, P. Hofmann, S. Ulstrup, Phys. Rev. B 100 (2019) 235423.

[68] F. Boschini, D. Bugini, M. Zonno, M. Michiardi, R.P. Day, E. Razzoli, B. Zwartsenberg, M. Schneider, E.H. da Silva Neto, S. dal Conte, S.K. Kushwaha, R.J. Cava, S. Zhdanovich, A.K. Mills, G. Levy, E. Carpene, C. Dallera, C. Giannetti, D.J. Jones, G. Cerullo, A. Damascelli, New J. Phys. 22 (2020) 023031.

[69] F. Bussolotti, H. Kawai, S.L. Wong, K.E.J. Goh, Phys. Rev. B 99 (2019) 045134.

[70] S. Ulstrup, J. Katoch, R.J. Koch, D. Schwarz, S. Singh, K.M. McCreary, H.K. Yoo, J. Xu, B.T. Jonker, R.K. Kawakami, A. Bostwick, E. Rotenberg, C. Jozwiak, ACS Nano 10 (2016b) 10058.

[71] P. Chen, W. Xu, Y. Gao, J.H. Warner, M.R. Castell, ACS Appl. Nano Mater. 1 (2018) 6976.

[72] M.-H. Chiu, C. Zhang, H.-W. Shiu, C.-P. Chuu, C.-H. Chen, C.-Y.S. Chang, C.-H. Chen, M.-Y. Chou, C.-K. Shih, L.-J. Li, Nature Commun. 6 (2015) 7666.

[73] C. Kastl, C.T. Chen, R.J. Koch, B. Schuler, T.R. Kuykendall, A. Bostwick, C. Jozwiak, T. Seyller, E. Rotenberg, A. Weber-Bargioni, S. Aloni, A.M. Schwartzberg, 2D Mater. 5 (2018) 045010.

[74] H.-W. Guo, Z. Hu, Z.-B. Liu, J.-G. Tian, Adv. Funct. Mater. 31 (2021) 2007810.

[75] J. Maklar, S. Dong, S. Beaulieu, T. Pincelli, M. Dendzik, Y.W. Windsor, R.P. Xian, M. Wolf, R. Ernstorfer, L. Rettig, Rev. Sci. Instrum. 91 (2020) 123112.

[76] J. Madéo, M.K.L. Man, C. Sahoo, M. Campbell, V. Pareek, E.L. Wong, A. Al-Mahboob, N.S. Chan, A. Karmakar, B.M.K. Mariserla, X. Li, T.F. Heinz, T. Cao, K.M. Dani, Science 370 (2020) 1199 LP.